Dynamic modelling of slip in a wind turbine spherical roller main bearing

Elisha de Mello[1*], Edward Hart[2], Yi Guo[3], Jonathan Keller[3], Rob Dwyer-Joyce[1] and Ampea Boateng[4]

[1]Leonardo Centre for Tribology, Mechanical Engineering, University of Sheffield, Sheffield, UK.
[2]Wind Energy and Control Centre, Electronic and Electrical Engineering, University of Strathclyde, Glasgow, UK.
[3]National Renewable Energy Laboratory, Golden, CO, USA.
[4]Offshore Renewable Energy Catapult, Blyth, UK.

*Corresponding author(s). E-mail(s): elxdemello1@sheffield.ac.uk;
Contributing authors: edward.hart@strath.ac.uk; yi.guo@nrel.gov; jonathan.keller@nrel.gov; r.dwyer-joyce@sheffield.ac.uk; ampea.boateng@ore.catapult.org.uk;

Abstract

This paper considers the problem of the dynamic modelling of macroslip in spherical roller bearings. By revisiting the fundamental physics which drive these systems, potential issues in existing models have been identified. Furthermore, in pure rolling conditions it was found that governing differential equations become "stiff", requiring the use of implicit methods of time integration. The problem of individual roller macroslip in a wind turbine main bearing is then investigated

This is a peer-reviewed, author's accepted manuscript of the following research article:
de Mello, E., Hart, E. J., Guo, Y., Keller, J., Dwyer-Joyce, R., & Boateng, A. (Accepted/In press).
Dynamic modelling of slip in a wind turbine spherical roller main bearing.
Forschung im Ingenieurwesen

using a simplified representation of system dynamics. Model results indicate clear links between slip/friction and the operational thrust strategy of the wind turbine, as well as significantly higher frictional effects in the downwind main bearing row. Due to modelling simplifications, these results should not yet be considered conclusive; further work is required.

Keywords: Rolling bearing, slip, dynamics, main bearing, wind turbine

1 Introduction

Wind turbine main bearings are receiving increased research scrutiny due to higher than expected failure rates [1–3], the root cause or causes of which have not yet been conclusively identified [4]. As wind turbines grow in size and wind farms move further offshore, component reliability becomes increasingly important in the context of the levelised cost of energy. Most main bearing failures are problematic in this regard, since they lead to significant loss of revenue from turbine downtime and necessitate the use of expensive jack-up vessels to remove and support the wind turbine rotor during changeovers. Furthermore, as turbines grow in size, the main bearing will increasingly become part of the load-carrying structure [3]. Access and replacement will thus be more difficult, meaning cost implications of failures are more severe. The above indicates that the identification and investigation of key underlying mechanisms of premature main bearing failures could result in significant improvements to main bearing reliability and design practises, in turn reducing the levelised cost of wind energy.

Slip, the presence of relative motion at contacting surfaces, can be a driver for a number of damage mechanisms in rolling element bearings. For example:

- Slip introduces frictional shear stresses which increase bulk stress values and pull the maximum stress closer to the surface, heightening the risk of surface-initiated fatigue[5].
- Slip is known to be a contributing factor to white etching cracks (WECs) in gearbox bearings [6], with WECs in main bearings now also being reported [7, 8].

- Smearing/adhesive wear may occur if slip coincides with asperity contact [8, 9].

Slip may occur at a micro-level, as a result of contact geometries under load, or at a macro-level, as a result of system dynamics. The focus of the current study is dynamically induced macroslip. *Cage slip* refers to instances where macroslip is such that the full rolling element set orbits the bearing centre at a speed which differs from that of pure rolling (therefore resulting in a cage speed which also differs). Macro-level *individual roller slip* also occurs, in addition to cage slip, as rollers enter and exit the loaded zone [8] or are otherwise affected by changes in system loading and speed. Importantly, individual roller slip will still occur in the absence of cage slip. A recent study investigated cage slip in the main bearing of an operational wind turbine as a possible contributor to premature failures [10]. The analysis concluded that levels of cage slip appeared negligible, likely as a result of high loads and single-cage design between bearing rows, but it was emphasised that individual roller slip may still be present. The current study seeks to build on this previous work by investigating individual roller macroslip in a wind turbine main bearing under realistic operating conditions, in which rapid variations in main bearing load magnitudes and directions are known to occur [11]. In order to computationally analyse this phenomenon, it is necessary to first develop an appropriate dynamic model. As will be described, this transpires to be non trivial. A detailed model derivation, along with careful treatment of some subtleties which arise, is therefore the initial focus of this paper. Results under realistic wind turbine operating conditions are then presented and discussed.

2 Background

2.1 General equations of motion for the rotation of a rigid body

Roller orbital dynamics in the developed model will be captured using rigid-body equations of motion. Note, this approximation is applied only with respect to the dynamic equations themselves. In contrast, all load and contact evaluation aspects of the model do incorporate elastic deflections using Hertzian theory (see Section 3.2). The rigid-body approximation in the context of dynamic equations is valid since the elastic deformations occurring in such

bearings are several orders of magnitude less than the geometric dimensions which determine inertia and momentum.

The fundamental equation of motion governing the rotation of a rigid-body is,

$$\sum_i \mathbf{M}_i = \frac{d\mathbf{L}}{dt}, \tag{1}$$

where the $\mathbf{M}_i$ are moments and $\mathbf{L}$ is the body's angular momentum (both vector quantities). However, this is the case only in an *inertial* frame of reference. As will be seen, it can often be beneficial to express $\mathbf{L}$ in a reference frame whose orientation changes in time, *i.e.* a rotating (*non-inertial*) reference frame. In such cases, the time-rate-of-change of the reference frame basis vectors must be taken into account. The body's angular momentum, $\mathbf{L}$, is the product of its 3×3 moment of inertia tensor, I, with its angular velocity vector, $\boldsymbol{\omega}$. In a non-rotating frame, I will in general be non-diagonal and time-dependent. If, instead, the reference frame rotates such that its axes maintain the same alignment with respect to the body's mass distribution throughout, I (as observed in the rotating frame) remains constant. If, in addition, this alignment coincides with the body's principal axes of inertia, I will also be diagonal here, $I = I_p$. Let $\boldsymbol{\Gamma}$ denote a choice of reference frame angular velocity which achieves both of these outcomes. It can be shown that,

$$\frac{d\mathbf{L}}{dt} = I_p\left(\frac{d\boldsymbol{\omega}}{dt} - \boldsymbol{\Gamma}\times\boldsymbol{\omega}\right) + \quad \boldsymbol{\Gamma}\times\mathbf{L}. \tag{2}$$

Expressing all vector/tensor quantities in the inertial (non-rotating) reference frame which has the same orientation as the rotating frame at each given instant in time (in this orientation $I = I_p$):

$$\mathbf{M}_i = \begin{bmatrix} M_{i,1} \\ M_{i,2} \\ M_{i,3} \end{bmatrix}, \quad \boldsymbol{\omega} = \begin{bmatrix} \omega_1 \\ \omega_2 \\ \omega_3 \end{bmatrix}, \quad \frac{d\boldsymbol{\omega}}{dt} = \begin{bmatrix} \dot{\omega}_1 \\ \dot{\omega}_2 \\ \dot{\omega}_3 \end{bmatrix}, \quad \boldsymbol{\Gamma} = \begin{bmatrix} \Gamma_1 \\ \Gamma_2 \\ \Gamma_3 \end{bmatrix}, \quad \mathbf{L} = I_p\boldsymbol{\omega} = \begin{bmatrix} I_1\omega_1 \\ I_2\omega_2 \\ I_3\omega_3 \end{bmatrix}. \tag{3}$$

Combining Equations 1 and 2, the equations of motion for rigid-body rotation under these circumstances are therefore,

$$\sum_i M_{1,i} = I_1\dot{\omega}_1 - I_2\Gamma_3\omega_2 + I_3\Gamma_2\omega_3 - I_1\left[\boldsymbol{\Gamma}\times\boldsymbol{\omega}\right]_1 \tag{4}$$

$$\sum_i M_{2,i} = I_2\dot{\omega}_2 - I_3\Gamma_1\omega_3 + I_1\Gamma_3\omega_1 - I_2\left[\boldsymbol{\Gamma}\times\boldsymbol{\omega}\right]_2 \tag{5}$$

$$\sum_i M_{3,i} = I_3\dot{\omega}_3 - I_1\Gamma_2\omega_1 + I_2\Gamma_1\omega_2 - I_3\left[\boldsymbol{\Gamma}\times\boldsymbol{\omega}\right]_3 \quad (6)$$

One possible suitable rotating frame can be obtained by fixing the frame in the rigid body so they rotate together in all dimensions. In such cases $\boldsymbol{\Gamma} = \boldsymbol{\omega}$, $\boldsymbol{\Gamma}\times\boldsymbol{\omega} = \boldsymbol{\omega}\times\boldsymbol{\omega} = 0$, and Equations 4–6 reduce to the well known *Euler's equations* of rigid-body rotation. However, in the current problem, it transpires that it is convenient to define a rotating frame for which $\boldsymbol{\Gamma} \neq \boldsymbol{\omega}$.

2.2 Angular momentum decomposition and the parallel axis theorem

The angular momentum, $\mathbf{L}$, of a rigid body with respect to the origin, $\mathcal{O}$, of an inertial reference frame may be shown to decompose as follows [12],

$$\mathbf{L} = \mathbf{L}_{\mathrm{CoM}} + \tilde{\mathbf{L}}, \quad (7)$$

where $\mathbf{L}_{\mathrm{CoM}}$ is the angular momentum of the body's centre of mass relative to $\mathcal{O}$[1], and $\tilde{\mathbf{L}}$ is the angular momentum of the rigid body relative to its centre of mass. Consider the simple case of rotation within a single plane, where an object (of mass m and in-plane moment of inertia I about its centre of mass) spins about its own centre of mass with angular velocity ω, while orbiting the stationary system origin (at a distance r) with angular velocity Ω. The above decomposition in this instance becomes,

$$L = mr^2\Omega + Iw. \quad (8)$$

A related result is the *parallel axis theorem*. This states that the moment of inertia of a rigid body about a given axis is equal to the sum of 1) its moment of inertia about the parallel axis which passes through the body's centre of mass, and 2) the product of the body's mass and the square of the distance between parallel axes [12]. For the simple case considered above, the parallel axis theorem gives,

$$I_{\mathcal{O}} = mr^2 + I. \quad (9)$$

This theorem deals with strict rigid-body rotation about the given axis. The implication being that for a parallel axis located outside of

[1] More specifically, $\mathbf{L}_{\mathrm{CoM}}$ is the angular momentum (relative to $\mathcal{O}$) of a point mass with mass equal to that of the rigid body, and with position and velocity equal to the body centre of mass at each point in time.

the body, the body maintains its initial orientation with respect to the origin at all times[2]. In cases where this occurs, the parallel axis theorem actually follows as a specific case of Equation 8, since one may easily show that $\omega = \Omega$ here. Crucially, the parallel axis theorem is not applicable in more general cases where the orbiting body may experience $\omega \neq \Omega$. In such instances the general form, Equation 7 or 8, must be used.

2.3 Bearing slip modelling in the literature

Much work on the modelling and analysis of slip in roller bearings has been undertaken in the literature [13–18]. This is usually in the context of cage slip. Particularly relevant to the current work is [13], where an efficient model is presented for the purposes of studying ball-bearing slip behaviour in wind turbine gearboxes. It is this previous paper on which the current modelling work is broadly based. A drawback of the model in [13] is the use of the parallel axis theorem, to arrive at the differential equation governing ball-bearing orbital speeds, since this theorem does not apply to bearing balls or rollers which themselves have independent velocity components about an axis parallel to that they are orbiting (see Section 2.2). It appears that the true angular momentum in the system was thus not being accounted for. The formulation used in [13] allows orbital motion and roller spin to be decoupled, greatly simplifying the solving process. However, considering the total system angular momentum (Equation 7 or 8) reveals that these quantities are in fact not decoupled. Similar issues related to system angular momentum characterisation and the coupling/decoupling of orbit and spin appears to be present in a number of models presented in the literature [14–17].

2.4 Numerical integration

The dynamic equations to be integrated in this work are second order. Such equations may be reformulated as a system of first-order differential equations for solving. Such systems are of the form,

$$\frac{d\mathbf{Y}}{dt} = f(\mathbf{Y}, t). \tag{10}$$

Integration may then be undertaken using any of a variety of numerical procedures of varying complexities, stabilities and accuracies.

[2] An example of such an orbit being that of our tidally locked moon.

With respect to stability, if a system of ordinary differential equations is "stiff" [19], explicit methods of integration are unstable unless the time step is made prohibitively small. In such cases, an implicit method must be used. The most basic numerical integrators falling into each category are the (explicit) Euler method,

$$\mathbf{Y}(t+dt) = \mathbf{Y}(t) + dt \cdot f(\mathbf{Y}(t), t), \tag{11}$$

and (implicit) backward Euler method,

$$\mathbf{Y}(t+dt) = \mathbf{Y}(t) + dt \cdot f(\mathbf{Y}(t+dt), t+dt). \tag{12}$$

In backward Euler, $\mathbf{Y}(t+dt)$ appears on both side of the equation. As such, each integration step requires an additional numerical procedure to solve for the $\mathbf{Y}(t+dt)$ which satisfies Equation 12. Improved stability therefore comes at a computational cost.

3 Methodology

3.1 Equations of motion for a spherical roller bearing

Reference frames used in the current work are shown in Figure 1. The bearing-centre frame is denoted by X_0, Y_0, Z_0. Roller-centric frames are denoted by x, y, z. Subscript "0" (e.g. x_0) indicates axes which translate with the roller centre, but which do not rotate and so maintain their initial orientation with the bearing-centre axes. The x, y, z axes (no sub- or super scripts) translate with the roller centre, while also rotating such that the y-axis remains aligned with the line from the bearing centreline to the centre of the roller. Primed axes (e.g. y', y'_0) are obtained from their unprimed counterparts by applying a rotation of α (the bearing contact angle) about the corresponding x-axis (x or x_0). Assuming no skewing or tilting of rollers occurs, and approximating the contact angle as remaining constant, a constant and diagonal moment of inertia tensor is seen in the described (rotating) x', y', z' frame. Note, a rotating frame is necessary to achieve this, as demonstrated by the changing mass distribution observable in the x'_0, y'_0, z'_0 frame (see Fig. 1c) as the roller orbits the bearing centreline. Other notation is as follows: ω (appropriately subscripted) will denote roller angular velocity in the various x, y, z frames. Γ will denote the angular velocity of the roller-centric rotating frame in the

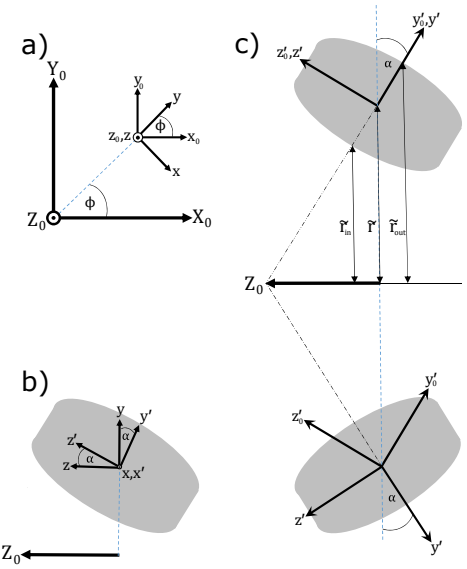

Fig. 1 Spherical roller bearing reference frames shown for a single row and roller.

various x, y, z frames. Ω will denote the orbital angular velocity of the roller centre in the X_0, Y_0, Z_0 frame.

Each roller in the bearing will rotate about its own centre, while also orbiting the bearing centreline. The roller is assumed to rotate freely (subject to moments in the system) only about z', and the roller centre is assumed to rotate only about Z_0. Rotation of the roller about other axes is assumed to be that which ensures the roller follows its design trajectory. The radius of orbit is assumed to remain constant throughout, as is the contact angle α. From the orientation described for the x, y, z frame, it follows that this frame is rotating with angular velocity $\mathbf{\Gamma}_{xyz} = [0, 0, \Omega_{Z_0}]^T$. It follows that the x', y', z' frame is rotating with angular velocity $\mathbf{\Gamma}_{x'y'z'} = [0, -\sin\alpha\ \Omega_{Z_0}, \cos\alpha\ \Omega_{Z_0}]^T$. Approximating the roller as a cylinder, the diagonal moment of inertia tensor in this frame is,

$$I_{x'y'z'} = \begin{bmatrix} \frac{1}{4}mr^2 + \frac{1}{12}ml^2 & 0 & 0 \\ 0 & \frac{1}{4}mr^2 + \frac{1}{12}ml^2 & 0 \\ 0 & 0 & \frac{1}{2}mr^2 \end{bmatrix}, \qquad (13)$$

where m is roller mass, r is the roller centreline radius and l is roller length. For roller slip analysis, $\omega_{z'}$ is the critical angular velocity

component. Since off-design skew and tilt are both assumed not to occur, the roller angular velocity components $\omega_{x'}$ and $\omega_{y'}$ are predetermined, since they must be such that the roller follows its design trajectory and orientation while orbiting the bearing centreline. Since the roller experiences a constant contact angle, α, it follows that $\omega_{x'} = 0$ throughout. $\omega_{y'}$ is nonzero, and a function of Ω_{Z_0} and bearing geometry. But, as will be shown, $\omega_{y'}$ turns out not to be needed. Since $\omega_{x'}$ and $\omega_{y'}$ may be considered known, only a single differential equation is required to be solved, that of $\omega_{z'}$ (Equation 6). It has been shown that,

$$\boldsymbol{\omega}_{x'y'z'} = \begin{bmatrix} 0 \\ \omega_{y'} \\ \omega_{z'} \end{bmatrix} \quad \text{and} \quad \boldsymbol{\Gamma}_{x'y'z'} = \begin{bmatrix} 0 \\ -\sin\alpha\ \Omega_{Z_0} \\ \cos\alpha\ \Omega_{Z_0} \end{bmatrix}, \tag{14}$$

hence,

$$I_{x'x'}\Gamma_{y'}\omega_{x'} = I_{y'y'}\Gamma_{x'}\omega_{y'} = I_{z'z'}\left[\boldsymbol{\Gamma}_{x'y'z'} \times \boldsymbol{\omega}_{x'y'z'}\right]_{z'} = 0. \tag{15}$$

The roller-centric differential equation to be solved in this case is therefore much simplified,

$$\sum_i M_{z',i} = I_{z'z'}\dot{\omega}_{z'}. \tag{16}$$

Note, while this equation initially appears to be independent of the roller orbital speed, Ω_{Z_0}, and the inner-raceway/shaft angular velocity, Ω_{in}, both quantities will influence $\omega_{z'}$ values through the moments acting on the roller. This will be shown explicitly in a later section. The roller's orbital motion about the bearing centreline, Ω_{Z_0}, is governed by a second differential equation, obtained using Equation 8 and roller velocity projections onto the z-axis. This takes the form,

$$\sum_i M_{Z_0,i} = mr^2\dot{\Omega}_{Z_0} + I_{zz}\big(\cos(\alpha)\dot{\omega}_{z'} - \sin(\alpha)\dot{\omega}_{y'}\big), \tag{17}$$

where I_{zz} is the lower diagonal element of $I_{x'y'z'}$ after transformation (using rotation matrices) to the x, y, z frame. Equation 17 shows explicitly the coupling between "roller orbit" and "roller spin" components.

3.2 Moments acting on a roller

Integrating rotational equations of motion requires the moments acting on the system to be resolved at each time step. Bearing roller moments are caused by tractive/friction forces which result from normal forces at roller-raceway and roller-cage contacts. The various forces acting on the roller are shown in Figure 2. These are as follows:

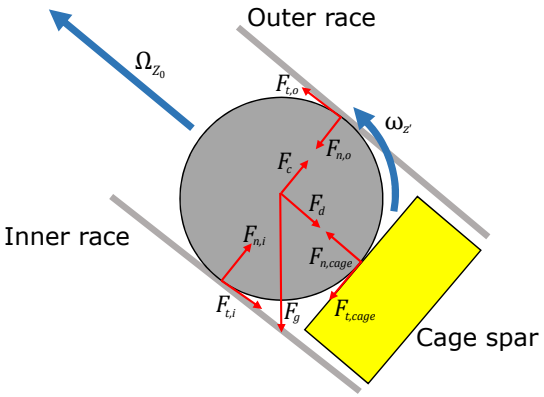

Fig. 2 Forces acting on an individual roller.

1. Gravitational force, $\mathbf{F}_g$. In the roller frame,

$$F_{g,x'} = mg\cos\phi \tag{18}$$
$$F_{g,y'} = -mg\cos\alpha\sin\phi \tag{19}$$
$$F_{g,z'} = -mg\sin\alpha\sin\phi \tag{20}$$

   where m is roller mass, g is acceleration due to gravity, α is the roller contact angle, and ϕ is the roller orbital position (see Fig. 1).
2. Centrifugal force, $\mathbf{F}_c$. In the roller frame,

$$F_{c,x'} = 0 \tag{21}$$
$$F_{c,y'} = m\Omega_{Z_0}^2\tilde{r}\cos\alpha \tag{22}$$
$$F_{c,z'} = m\Omega_{Z_0}^2\tilde{r}\sin\alpha, \tag{23}$$

where $\tilde{r}$ is the vertical height from the bearing centreline to the roller centre (see Fig. 1).

3. Fluid (lubricant) resistance drag, $\mathbf{F}_d$. In the roller frame,

$$F_{d,x'} = \text{sign}(v)\frac{1}{2}\rho\epsilon v^2 C_D A \tag{24}$$

$$F_{d,y'} = 0 \tag{25}$$

$$F_{d,z'} = 0, \tag{26}$$

where $v = \Omega_{Z_0}\tilde{r}$ is the roller tangential velocity in the bearing frame, ρ is lubricant density, $\epsilon = 0.7$ is a fill factor, A is the cross-sectional area of the roller, and C_D is the drag coefficient (taken to be 1 based on approximate Reynolds numbers for the system).

4. Inner- and outer-raceway normal contact forces, $\mathbf{F}_{n,i}$ and $\mathbf{F}_{n,o}$, respectively. These forces consist of a y' component only, and are approximated as follows: first a Hertzian contact model (essentially identical to that of [11], but containing discrete representations of rollers) of the bearing is used to perform a static load balance which determines the normal load on each roller required to balance the current bearing load; second, the magnitude of the unbalanced resultant y' body force, $F_{g,y'} + F_{c,y'}$, is added to the appropriate raceway to balance all non-tractive forces along y'. Hertzian theory is then used to determine the resulting contact patch and pressure distribution, if present, at each contact location (required for traction force estimation).
5. The form of the cage normal force, $\mathbf{F}_{n,cage}$, will differ depending on the model implementation. In the current work, the normal cage force will be used to act as a "control" in the system since, ultimately, it will be assumed that it acts to balance all roller forces along x' (see Section 3.3). Similar to raceway normal forces, Hertzian theory is used to evaluate the contact patch and pressure distribution between roller and cage. The cage is assumed to conform to the roller with the same geometry as between roller and raceways in the lateral direction. In the rolling direction the cage is assumed to also conform to the roller with equal percentage conformity to that defined laterally. Note, in the applied formulation the cage tractive force represents an unbalanced y' force in the system; however, testing has revealed this unbalanced force to be acceptably small.
6. Elastohydrodynamic tractive forces ($\mathbf{F}_{t,i}$, $\mathbf{F}_{t,o}$, $\mathbf{F}_{t,cage}$) at inner-raceway, outer-raceway and cage contacts, respectively. These are

generated from shearing of the lubricant film when slip is present which, in turn, results in surface-stress distributions over each contact patch. At the point (x'_p, z'_p) in a contact patch, the shear stress (τ) in a Newtonian fluid separating the two surfaces may be approximated as [20],

$$\tau(x'_p, z'_p) = \frac{\eta(x'_p, z'_p)\Delta u}{h_c}, \tag{27}$$

where η is the lubricant dynamic viscosity (both pressure and temperature dependent), Δu is the slip speed, and h_c is the central film thickness. Since the main focus here is macro-level slip, microslip effects are not included in the current form of this model. macroslip, Δu, was estimated at the roller centre based on unloaded bearing geometry (see below), with slip values across the contact patch approximated as being equal to this value. The viscosity across the contact patch is affected by local pressure variations and frictional heating which results from lubricant shearing. A closed-form approximation of viscosity variations under these conditions was derived by Crook [20] and also applied in [13]. The same approach is used again here, allowing shear stress values throughout the contact to be evaluated. Equation 27 is then integrated over the contact patch in order to obtain an estimate of the resultant surface tractive force at that interface. Lubrication analysis used a Barus law pressure-viscosity coefficient of 21 GPa^{-1}, a temperature-viscosity coefficient of 0.056 C^{-1}, lubricant thermal conductivity of 0.125 $\text{Jkg}^{-1}\text{K}^{-1}$, and a lubricant specific gravity of 0.9. The lubricant contact-inlet temperature was set at 35 C throughout. Other lubrication/bearing parameters match that of [21]. The central film thickness, h_c is evaluated using an equivalent line contact representation [21, 22] and a central film thickness formula which accounts for surface roughness [23]. Denoting roller and raceway/cage surface tangential velocities as u_1 and u_2, respectively. The above formulation requires both entrainment velocity, $u_e = \frac{1}{2} \mid u_1 + u_2 \mid$ and slip speed, $\Delta u = u_2 - u_1$, to be evaluated at each contact. For convenience, surface tangential velocity expressions were identified such that positive slip values result in a positive rotational acceleration of the roller in its local frame and, hence, generate roller moments

with the same sign as Δu. These velocities are as follows,

$$u_{2,in} = -(\Omega_{in} - \Omega_{Z_0})\tilde{r}_{in} \quad (28)$$

$$u_{2,out} = (\Omega_{out} - \Omega_{Z_0})\tilde{r}_{out} \quad (29)$$

$$u_{2,cage} = 0 \quad (30)$$

$$u_{1,in} = u_{1,out} = u_{1,cage} = \omega_{z'} r \quad (31)$$

r is the roller centreline radius. The bearing in question has a stationary outer-raceway, so $\Omega_{out} = 0$.

Having calculated the traction forces as described above for each case, the moments acting on the roller at each point in time are $\mathbf{M}_{t,i} = r\mathbf{F}_{t,i}$, $\mathbf{M}_{t,o} = r\mathbf{F}_{t,o}$, and $\mathbf{M}_{t,cage} = r\mathbf{F}_{t,cage}$.

3.3 Model implementation

Previous sections highlight the complexity of dynamics in the full system being considered, including the presence of coupled differential equations for $\omega_{z'}$ and Ω_{Z_0}. Previous work outlined in Section 1 indicates that some simplification may be possible since, due to the absence of cage slip, it appears reasonable to assume roller orbital trajectories are maintained at that of pure rolling[3] via cage normal forces (neglecting clearance between cage spars and rollers). However, even then one would have to ensure that forces/moments are such that both Equation 16 and 17 remain satisfied throughout, a task which is not obviously straightforward. Furthermore, under high loads which (locally) drive rollers at their pure rolling speed, it has been found that governing differential equations become stiff, requiring an additional solving procedure at each time-step. Based on the above difficulties, which would require complex nested iterative solving to handle all aspects of the real-world problem, it was deemed sensible to first consider a simplified version of the system which is analogous, but not identical, to the original. We therefore consider the case where rollers are subject to identical loading, contact geometries, entrainment speeds and surface tangential velocities as those seen in the main bearing (as per Section 3.2), but where all of this occurs for rollers travelling in a straight line at velocity $\Omega_{Z_0}\tilde{r}$ (for Ω_{Z_0} set equal to the orbital speed under pure rolling) between parallel raceways, as opposed to orbiting a bearing centre. In this

[3]The benefit of this being that at "pure rolling" the orbital speed becomes a simple function of shaft speed, similar to a gear-speed equation [11, 21].

simplified case, there is no longer an orbital component to angular momentum, and hence Equation 17 falls away, leaving the single differential equation, Equation 16, to be integrated. While not identical to the real-world problem, it is believed that analysis of this simplified case will still provide insights into the key mechanisms at play in such systems. Additionally, wind turbine rotors have large rotational inertia, and so is it assumed that $\dot{\Omega}_{Z_0}\tilde{r}$ is small/negligible. The cage normal force for each roller is therefore specified such that it balances the other forces acting along x',

$$F_{n,cage} = \mid F_{g,x'} + F_{d,x'} + F_{t,i} - F_{t,o} \mid . \tag{32}$$

Rollers in this system are therefore independent of one another, since they interact with their adjacent cage spars only. Thus, dynamic analysis may be undertaken considering just a single roller in the system. Applied load balancing via the Hertzian model still requires knowledge of the orbital position of all rollers, but (since Ω_{Z_0} is now that of pure rolling) orbital position over time may be easily determined, for example see [11].

This model implementation was undertaken using the main bearing and 1.5 MW wind turbine aeroelastic model applied in previous work [11, 21]. Simulated wind conditions contained a shear exponent of 0.2, and aeroelastic simulations were performed at three levels of kinematic turbulence (high - A, medium - B and low - C, as specified by IEC-61400 design standards). Simulations at each turbulence level were performed for turbulent wind fields with mean wind speeds of 12–24 m/s. In total, analysis of individual roller dynamics was therefore undertaken across 21 10-min turbine simulations. Note, all simulations fall within the turbine's second constant speed region, wherein pitch action is attempting to maintain the shaft speed at its set ratedlevel. The roller differential equation, Equation 16, remains stiff. Stable time integration was therefore achieved using the backward Euler method (an example of instability observed for an explicit integrator is provided in Appendix A).

3.4 Analysis metrics for individual roller slip

Appropriate metrics with which to analyse individual roller slip results are now considered. Importantly, each of the damage mechanisms described in Section 1 are not dependent on slip in isolation, but rather a combination of slip and surface friction. Indeed, if slip

occurs in the absence of friction then no damage will result. Analysis metrics should ideally reflect this reality, while also facilitating convenient comparative analyses across a range of simulations.

Occurrences of smearing damage within a contact have been linked to large instantaneous frictional power values [8], $P(t)$, where,

$$P(t) = \mid F_t(t) \cdot \Delta \dot{u}(t) \mid . \tag{33}$$

Related to this, WEC damage has been shown to correlate with the cumulative frictional energy, $E(t)$, at an interface [24, 25], where,

$$E(t) = \int_{t_0}^{t} P(t) \ \ dt = \int_{t_0}^{t} \mid F_t(t) \cdot \Delta \dot{u}(t) \mid \quad dt. \tag{34}$$

The above two quantities both fulfill the outlined criteria regarding useful metrics for roller slip analysis. Both $E(t)$ and $P(t)$ will therefore be used to analyse results. The cumulative energy is a particularly convenient measure, since it neatly summarises a full simulation's worth of results into a single number. Cumulative energy results presented in the following section will consider the total cumulative energy, *i.e.* $E_{tot} = E_{in} + E_{out} + E_{cage}$. As will be described, E_{tot} values were found to be dominated by E_{cage} here. Frictional power results will also be considered, in the form of the maximum power occurring per roller orbit. Within a single roller orbit, the maximum power is taken to be the largest value across all interfaces, *i.e.* $P_{max} = \max\left(E_{in,max},\ E_{out,max},\ E_{cage,max}\right)$.

It is reiterated that the focus of this paper is model development for individual roller slip in a wind turbine main bearing. As such, the above metrics are applied in order to facilitate a contextually appropriate analysis of model outputs, rather than necessarily seeking to assess the risk of any particular form of slip induced damage.

4 Results

Figure 3a shows the roller rotational speed, $\omega_{z'}$, solution having applied the model under conditions of a static downward load and constant speed, each set to the mean load and speed seen in the 14m/s mean wind speed case with turbulence level B. Roller rotational speeds can be seen to remain at pure rolling throughout the load zone. This is expected due to high contact forces. As the roller exits the load zone, the braking action of cage contact decelerates the

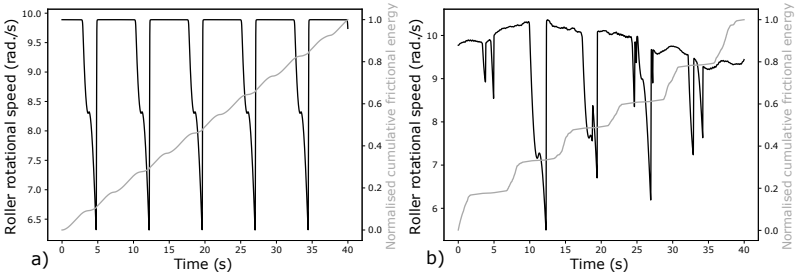

Fig. 3 a) Roller rotational speed and normalised cumulative frictional energy under constant load and speed, b) Roller rotational speed and normalised cumulative frictional energy under time-varying conditions.

roller. An inflexion point in rotational speed is visible. This occurs as the roller passes over the top of the bearing, where briefly no gravitational component is acting to push the roller into the cage. Upon reentering the loaded zone, the roller can be seem to rapidly re-accelerate to the pure-rolling speed. The total cumulative frictional energy from across all contacts (cage, inner- and outer-raceway) is also shown. This variable increases fairly steadily throughout the roller's orbit. As there is essentially no slip at inner- and outer-raceways towards the centre of the load zone, energy accumulation there is due to roller-cage interaction. Figure 3b provides results under time-varying conditions. Note, in this case the cumulative frictional energy values were around 2 orders of magnitude greater than in the static case. Here, the roller can be seen to track the slowly changing pure-rolling speed when loaded. Note, the bearing applied load is also changing in both magnitude and direction throughout. The majority of energy may be seen to accumulate towards the centre of the loaded zone. Again, this energy accumulation is dominated by friction between the roller and cage, resulting from (brief) differential traction forces at inner- and outer-raceways acting to force the roller into the cage spar. These raceway traction forces are present due to the slow variations in shaft speed, which in turn are changing the pure rolling speed. Traction forces therefore develop which drive the roller towards the new pure-rolling $\omega_{z'}$ value.

Cumulative frictional energies were compared across the wind speeds and turbulence levels, as shown in Fig. 4a. Frictional energy is seen to be highest at the lowest considered wind speeds of 12 and 14 m/s. This observation can be explained as resulting from turbine operation/control, since once rated power is reached at around 12

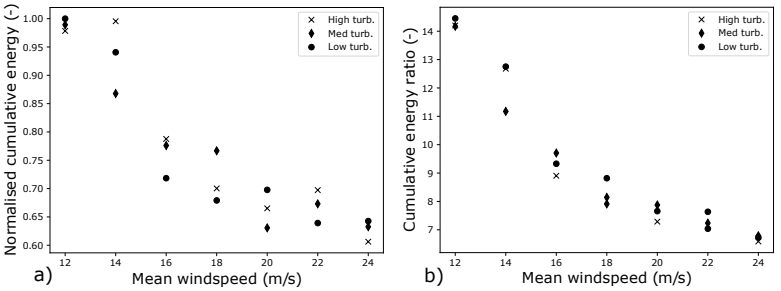

Fig. 4 a) Normalised cumulative frictional energies in the downwind row for each turbine simulation. Results are normalised against the 12 m/s, turbulence C result, b) Ratios of frictional energy results in the downwind versus upwind main bearing row, E_{down}/E_{up}.

m/s, excess energy and loads at higher wind speeds are shed by the control system pitching the blades. This results in design thrust loads which are maximal at about 12 m/s, and then fall continuously for higher wind speeds. As a result, higher frictional energies might well be expected at points of higher thrust loading. Further analysis is required before any definite links between frictional energy and turbulence level might be established. Discussions with wind farm

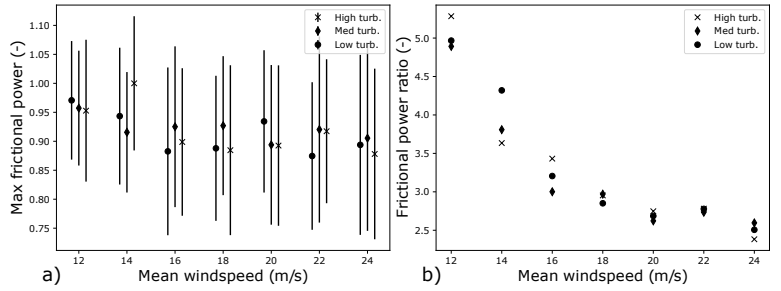

Fig. 5 a) Mean and standard deviation values for the maximum frictional power per roller orbit in the downwind row. Results are normalised against the 14 m/s, turbulence A result. Note, results are staggered about each mean wind speed for clarity, b) Ratios of mean values of max frictional power per orbit in the downwind versus upwind main bearing rows.

operators indicate that main bearing failures tend to occur in the downwind main bearing row. Frictional energy results were therefore consider for one roller in the downwind and one roller in the upwind row, to determine if any differences were predicted by this model.

Ratios of the downwind to upwind frictional energy values at each operating point are shown in Fig 4b. As shown, frictional energies across all wind speeds and turbulence levels were found to be around one order of magnitude higher in the downwind row, compared to the upwind row. This is likely due to the fact that the downwind row is more highly loaded in general as a result of supporting thrust [11, 26].

Frictional power values at contact interfaces were also analysed by extracting the maximum frictional power (across all three contact points) from each roller orbit about the main bearing, within a given simulation. Figure 5a shows means and standard deviations of the *maximum frictional power per roller orbit* in the downwind row at each operating point (results are staggered about each mean wind speed for clarity). In contrast to cumulative energy results, no definite trend is discernible. This indicates that large values of instantaneous frictional power may occur at any of the operating points considered here. The standard deviations of these results indicate that there are high levels of variability in the maximum power occurring per roller orbit. Differences between the frictional power seen in the downwind versus upwind row were also considered. Figure 5b shows ratios of the mean values of *maximum frictional power per roller orbit* in the downwind versus upwind main bearing rows. Here, a clear trend is present, with the highest bearing-row power discrepancies occurring at 12 m/s wind speeds and dropping off thereafter. As for the cumulative energy results, this appears to be linked to the thrust operating strategy of the wind turbine. Maximum frictional power values may be seen to be consistently as much as 5 times larger for a roller in the downwind row, compared to a roller in the upwind row.

It is emphasised that while the utilised model is arguably analogous to an operating main bearing, it is certainly not identical. Results presented here must therefore be interpreted with this in mind. In future work it will be important to consider the relevance of microslip, compared to the macroslip analysed here, as well as clearance between the rollers and cage spars. Consideration should also be given to integrating the true (coupled) equations of motion, Equations 16 and 17.

5 Conclusions

This work has considered the dynamic modelling of macroslip in spherical roller bearings. Equations of motion were presented in a fully generalised form which allows for the utilisation of any suitable rotating coordinate frame. Fundamental concepts of angular momentum characterisation in spinning-orbiting systems were also presented. Careful application of this theory allowed for the correct (coupled) system of dynamic equations to be identified, while also highlighting apparent errors in existing models. A simplified model for capturing individual roller macroslip behaviour in a wind turbine main bearing was then presented, which accounts for elastic contact and lubricant shearing effects. Additionally, it was demonstrated that rolling bearing equations of motion become "stiff" under certain conditions, requiring iterative approaches to time integration. The presented model was implemented, using input data obtained from turbulent aeroelastic wind turbine simulations, and results analysed via cumulative frictional energy and instantaneous frictional power metrics. Model results indicate clear links between slip/friction and the operational thrust strategy of the wind turbine, as well as significantly higher frictional effects in the downwind main bearing row. macroslip was predicted to be most directly relevant at roller-cage contacts, driven by differential friction forces on raceways as the roller tracks a slowly varying pure-rolling speed. Due to modelling simplifications, these results should not yet be considered conclusive. Further modelling and validation work is required, including the addition of: micro-slip effects, roller-cage clearance and integration of the fully coupled equations of motion for this system.

Acknowledgments. The authors would like to thank to Dr Tim Rogers (University of Sheffield) for helpful discussions which greatly supported this research. This work forms part of project AMBERS (Advancing Main-BEaRing Science for wind and tidal turbines). Elisha de Mello's PhD project is funded by the Powertrain Research Hub, co-funded by the Offshore Renewable Energy Catapult. Edward Hart is funded by a Brunel Fellowship from the Royal Commission for the Exhibition of 1851. This work was authored in part by the National Renewable Energy Laboratory, operated by Alliance for Sustainable Energy, LLC, for the U.S. Department of Energy (DOE) under Contract No. DE-AC36-08GO28308. Funding provided by the

U.S. Department of Energy Office of Energy Efficiency and Renewable Energy Wind Energy Technologies Office. The views expressed in the article do not necessarily represent the views of the DOE or the U.S. Government. The U.S. Government retains and the publisher, by accepting the article for publication, acknowledges that the U.S. Government retains a nonexclusive, paid-up, irrevocable, worldwide license to publish or reproduce the published form of this work, or allow others to do so, for U.S. Government purposes.

Appendix A Stiff differential equation example

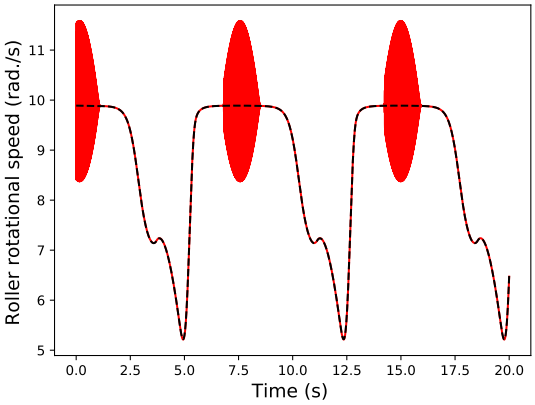

Fig. A1 Example of instability in the highly loaded zone when using Euler's method (red). Backward Euler (black) can be seen to avoid this instability issue.

References

[1] Hart, E., Turnbull, A., Feuchtwang, J., McMillan, D., Golysheva, E., Elliott, R.: Wind turbine main-bearing loading and wind field characteristics. Wind Energy **22**(11), 1534–1547 (2019)

[2] Hart, E., Clarke, B., Nicholas, G., Kazemi Amiri, A., Stirling, J., Carroll, J., Dwyer-Joyce, R., McDonald, A., Long, H.: A review

of wind turbine main bearings: design, operation, modelling, damage mechanisms and fault detection. Wind Energy Science **5**(1), 105–124 (2020)

[3] Nejad, A.R., Keller, J., Guo, Y., Sheng, S., Polinder, H., Watson, S., Dong, J., Qin, Z., Ebrahimi, A., Schelenz, R., *et al.*: Wind turbine drivetrains: state-of-the-art technologies and future development trends. Wind Energy Science **7**(1), 387–411 (2022)

[4] Guo, Y., Bankestrom, O., Bergua, R., Keller, J., Dunn, M.: Investigation of main bearing operating conditions in a three-point mount wind turbine drivetrain. Forschung im Ingenieurwesen **85**(2), 405–415 (2021)

[5] Kotzalas, M.N., Doll, G.L.: Tribological advancements for reliable wind turbine performance. Philosophical Transactions of the Royal Society A: Mathematical, Physical and Engineering Sciences **368**(1929), 4829–4850 (2010)

[6] Gould, B., Greco, A.: The influence of sliding and contact severity on the generation of white etching cracks. Tribology Letters **60**(2), 1–13 (2015)

[7] Greco, A., Demas, N., Erck, R., Gould, B., Keller, J., Sheng, S., Guo, Y.: Wind turbine drivetrain reliability. Technical Report PR–5000–84029, National Renewable Energy Lab.(NREL), Golden, CO (United States) (2022). https://www.nrel.gov/docs/fy23osti/84029.pdf

[8] Doll, G.: Surface engineering in wind turbine tribology. Surface and Coatings Technology, 128545 (2022)

[9] Brizmer, V., Stadler, K., van Drogen, M., Han, B., Matta, C., Piras, E.: The tribological performance of black oxide coating in rolling/sliding contacts. Tribology Transactions **60**(3), 557–574 (2017)

[10] Bergua Archeli, R., Keller, J., Bankestrom, O., Dunn, M., Guo, Y., Key, A., Young, E.: Up-tower investigation of main bearing cage slip and loads. Technical report, National Renewable Energy Lab.(NREL), Golden, CO (United States) (2021)

[11] Hart, E.: Developing a systematic approach to the analysis of time-varying main bearing loads for wind turbines. Wind Energy **23**(12), 2150–2165 (2020)

[12] Rao, A.: Dynamics of Particles and Rigid Bodies: a Systematic Approach. Cambridge University Press, ??? (2006)

[13] Jain, S., Hunt, H.: A dynamic model to predict the occurrence of skidding in wind-turbine bearings. In: Journal of Physics: Conference Series, vol. 305, p. 012027 (2011). IOP Publishing

[14] Tu, W., Shao, Y., Mechefske, C.K.: An analytical model to investigate skidding in rolling element bearings during acceleration. Journal of mechanical science and technology **26**(8), 2451–2458 (2012)

[15] Han, Q., Chu, F.: Nonlinear dynamic model for skidding behavior of angular contact ball bearings. Journal of Sound and Vibration **354**, 219–235 (2015)

[16] Han, Q., Li, X., Chu, F.: Skidding behavior of cylindrical roller bearings under time-variable load conditions. International Journal of Mechanical Sciences **135**, 203–214 (2018)

[17] Liu, Y., Chen, Z., Tang, L., Zhai, W.: Skidding dynamic performance of rolling bearing with cage flexibility under accelerating conditions. Mechanical Systems and Signal Processing **150**, 107257 (2021)

[18] Guo, Y., Keller, J.: Validation of combined analytical methods to predict slip in cylindrical roller bearings. Tribology International **148**, 106347 (2020)

[19] Wanner, G., Hairer, E.: Solving Ordinary Differential Equations II vol. 375. Springer, ??? (1996)

[20] Crook, A.: The lubrication of rollers III. A theoretical discussion of friction and the temperatures in the oil film. Philosophical Transactions of the Royal Society of London. Series A, Mathematical and Physical Sciences **254**(1040), 237–258 (1961)

[21] Hart, E., de Mello, E., Dwyer-Joyce, R.: Wind turbine main-bearing lubrication–part 2: Simulation-based results for a double-row spherical roller main bearing in a 1.5 mw wind turbine. Wind Energy Science **7**(4), 1533–1550 (2022)

[22] Hart, E., de Mello, E., Dwyer-Joyce, R.: Wind turbine main-bearing lubrication–part 1: An introductory review of elasto-hydrodynamic lubrication theory. Wind Energy Science **7**(3), 1021–1042 (2022)

[23] Masjedi, M., Khonsari, M.: Film thickness and asperity load formulas for line-contact elastohydrodynamic lubrication with provision for surface roughness. Journal of tribology **134**(1) (2012)

[24] Gould, B., Greco, A.: Investigating the process of white etching crack initiation in bearing steel. Tribology Letters **62**(2), 1–14 (2016)

[25] Vaes, D., Guo, Y., Tesini, P., Keller, J.A.: Investigation of roller sliding in wind turbine gearbox high-speed-shaft bearings. Technical report, National Renewable Energy Lab.(NREL), Golden, CO (United States) (2019)

[26] Guo, Y., Thomson, A., Bergua, R., Bankestrom, O., Erskine, J., Keller, J.: Acoustic emission measurement of a wind turbine main bearing. Technical report, National Renewable Energy Lab.(NREL), Golden, CO (United States) (2022)